Effects of Radiation Heating on Additively Printed Hybrid Fuel Grain Oxidizer-to-Fuel Ratio Shift

by

Stephen Merkley

A thesis submitted in partial fulfillment
of the requirements for the degree

of

Master of Science

in

Aerospace Engineering

Contents

- Small-Scale Hybrid Rocket Motors
- Fuel-Rich Behavior
- Oxidizer-to-Fuel (O/F) Ratio
- Fuel Regression Rate Model
- Experimental Set-up
- Results
- Conclusion
- Future Work

Traditional Hybrid Rockets

- Solid fuel, fluid oxidizer

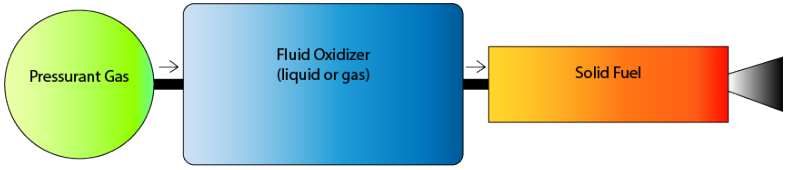

Hybrid Rocket Motor (HRM) Concept

- Cast and cure fuel
- Paraffin
- hydroxyl terminated polybutadiene
  - HTPB
- high density polyethylene
  - HDPE

Small-Scale Hybrid Rocket Motors

- 3D printed acrylonitrile butadiene styrene (ABS) as hybrid rocket fuel

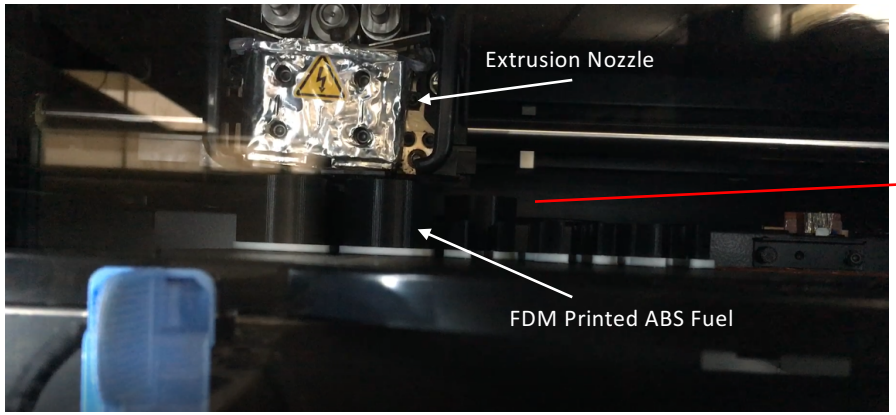

Additive Manufacturing

ABS Fuel

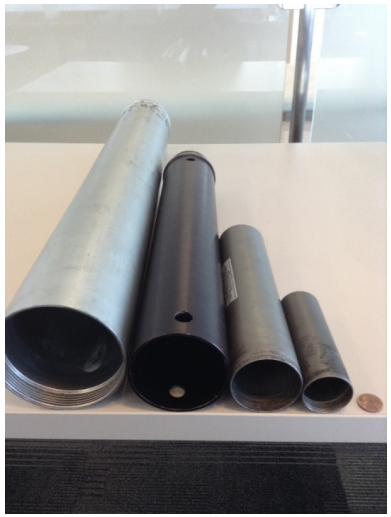

Motor Cases

Application

- Non-toxic, benign, and low cost small spacecraft propulsion

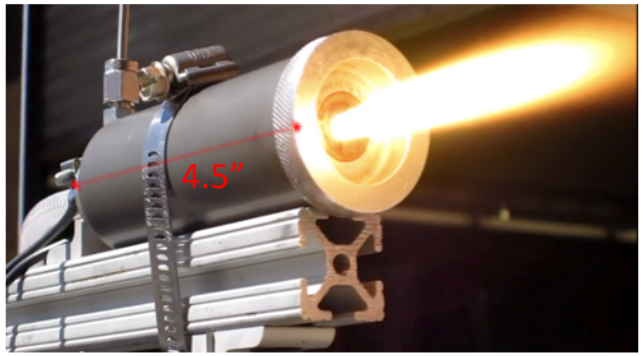

Small-Scale ABS/GOX Thruster

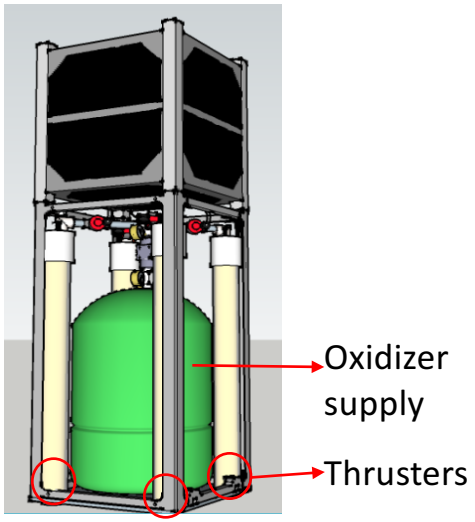

Small-Satellite Propulsion Unit Concept

Fuel-Rich Burn

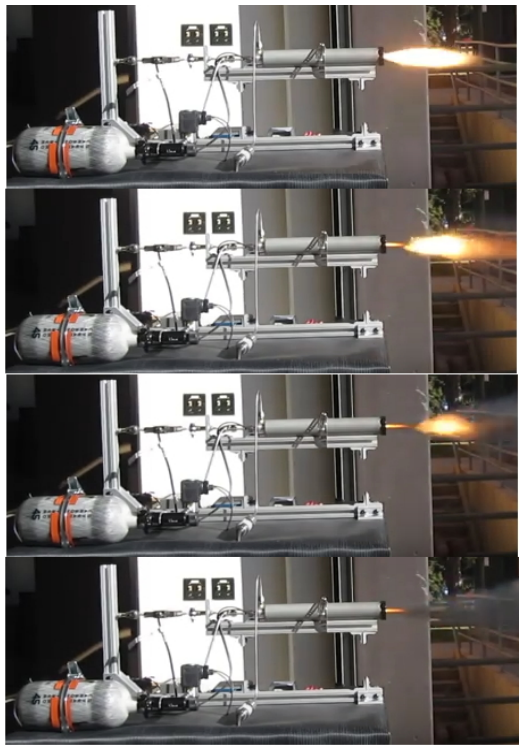

Image Sequence of 8-Second Burn with Small-Scale ABS/GOX Motor

- Small-scale motors using ABS and gaseous oxygen (GOX) exhibit progressively fuel-rich behavior
- https://www.youtube.com/watch?v=N-ZzLzdVP1A
- This implies that the oxidizer-to-fuel (O/F) ratio is decreasing through the duration of the burn

Chamber Pressure Profile and Qualitative Comparison

German STERN Program Paraffin/N_2O

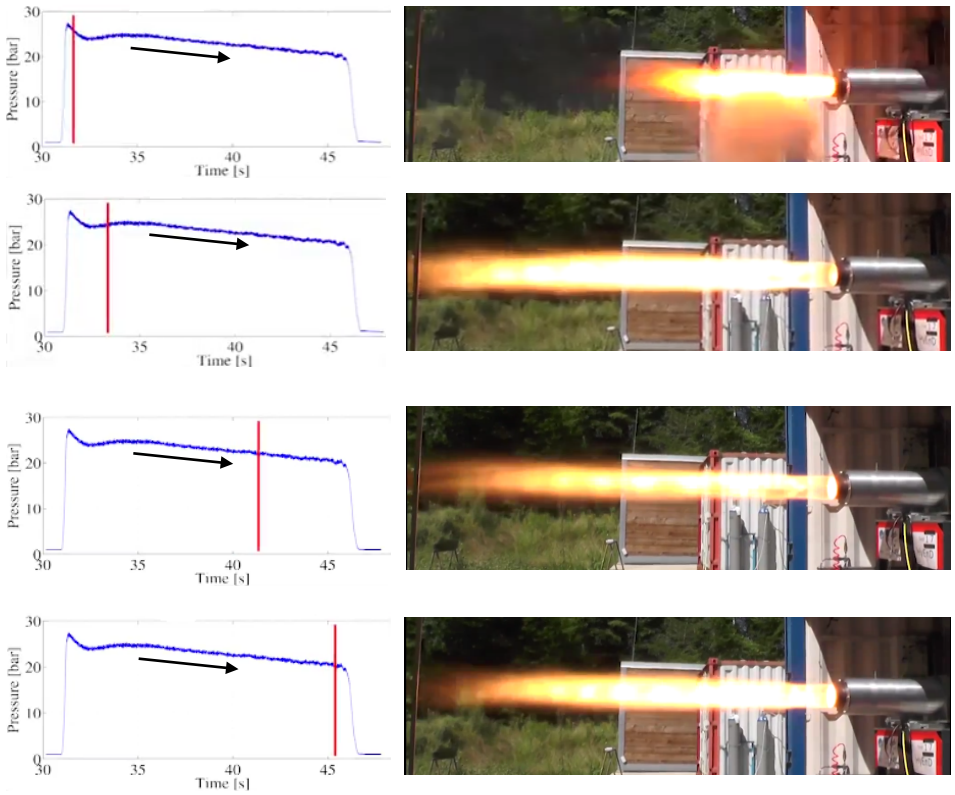

Utah State University ABS/GOX

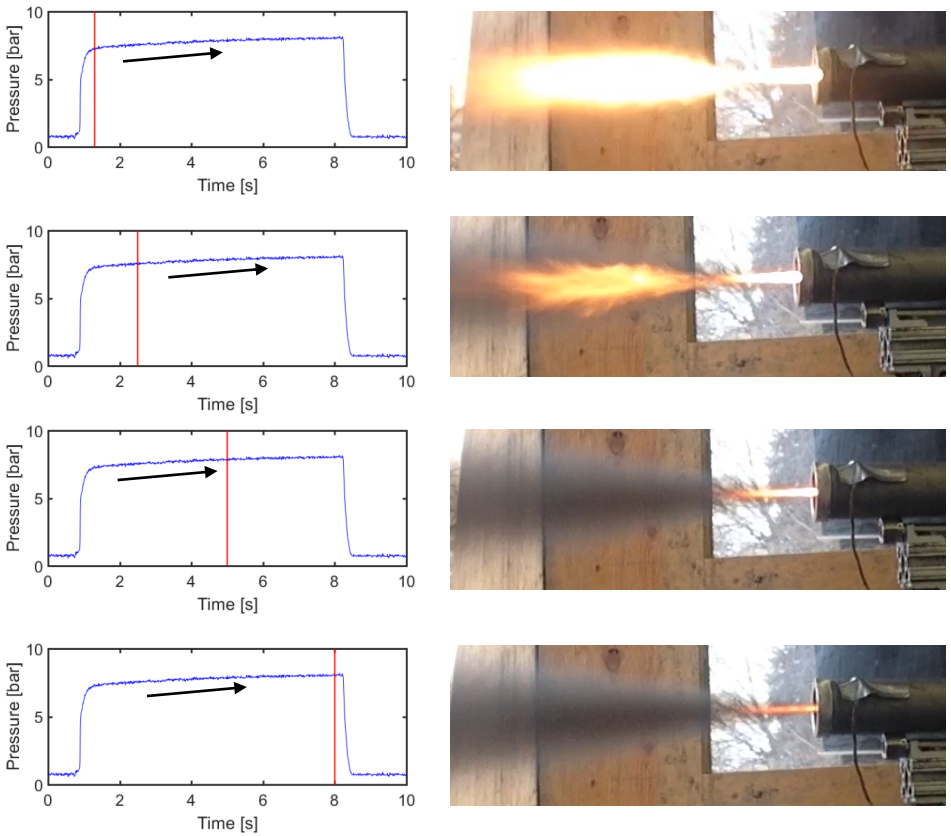

[rocketman0815]. (2016, August 15). *HyEnD – HyRES Hybrid Rocket Engine Test 17*. [Video File]. Retrieved from https://www.youtube.com/watch?v=KFEZ26gBhnE.

Oxidizer-to-Fuel (O/F) Ratio

- Ratio of oxidizer mass flow to fuel mass flow

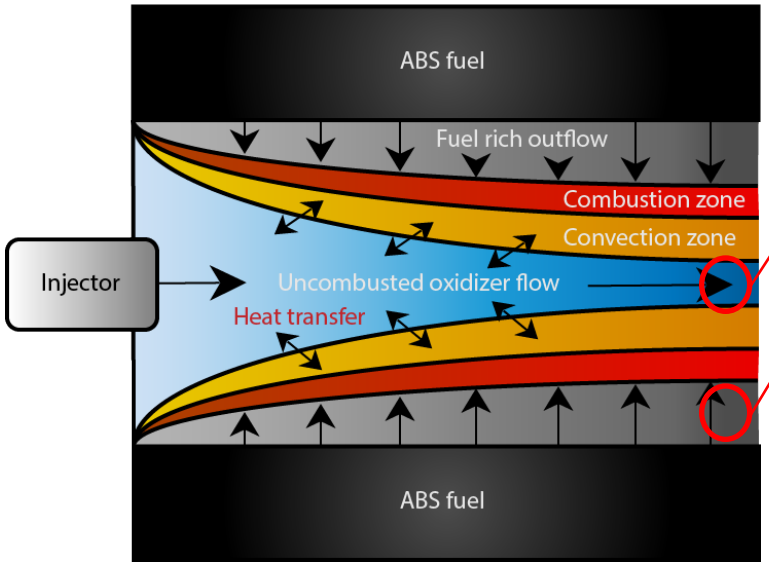

Hybrid Rocket Motor Combustion Concept
Based on Marxman Theory

$$\frac{Oxidizer\ mass\ flow}{Fuel\ mass\ flow} = \frac{\dot{m}_{ox}}{\dot{m}_f} = O/F$$

$$\frac{\dot{m}_{ox}}{\dot{m}_f} = \frac{\dot{m}_{ox}}{\rho_f A_b \dot{r}} = \frac{\dot{m}_{ox}}{\rho_f (\pi D_p L) \dot{r}}$$

- ρ_f, fuel density
- D_p, port diameter
- L, fuel length
- $\dot{r}$, fuel regression rate

- O/F ratio behavior depends on fuel regression rate

Fuel Regression Rate

- Linear rate of regression of the fuel normal to the surface gradient

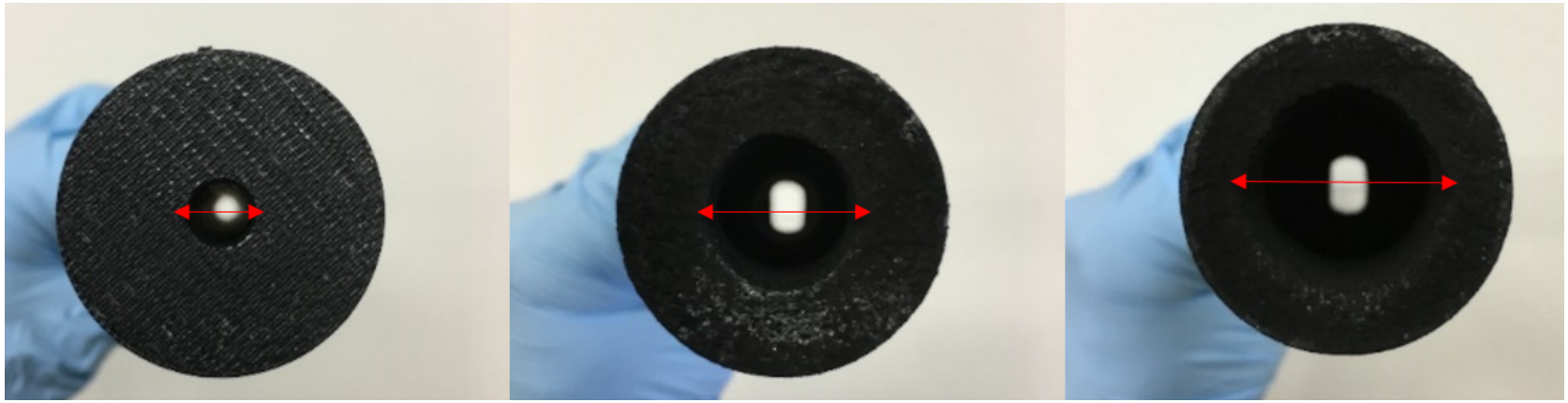

Cross-Sectional View of ABS Fuel Port Diameter Expansion

Empirical Model for Regression Rate

- Fuel regression rate is difficult to measure directly

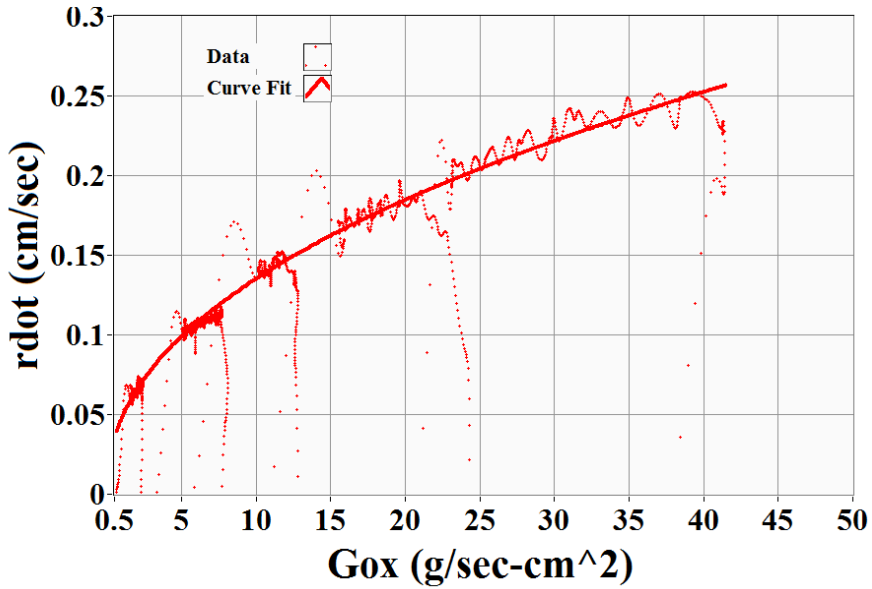

Curve-Fitting Fuel Regression Rate Data

- Experimental regression rate data is obtained indirectly from calculated propellant mass flow
- Curve-fit model, $\dot{r} = a \cdot G_{ox}^{n'}$
  - a, empirical scale factor
  - n', empirical exponent
  - G_{ox}, oxidizer mass flux
    - $G_{ox} = \frac{\dot{m}_{ox}}{A_c} = \frac{\dot{m}_{ox}}{\frac{\pi}{4}D_p^2}$

Curve-Fit Regression Rate Data

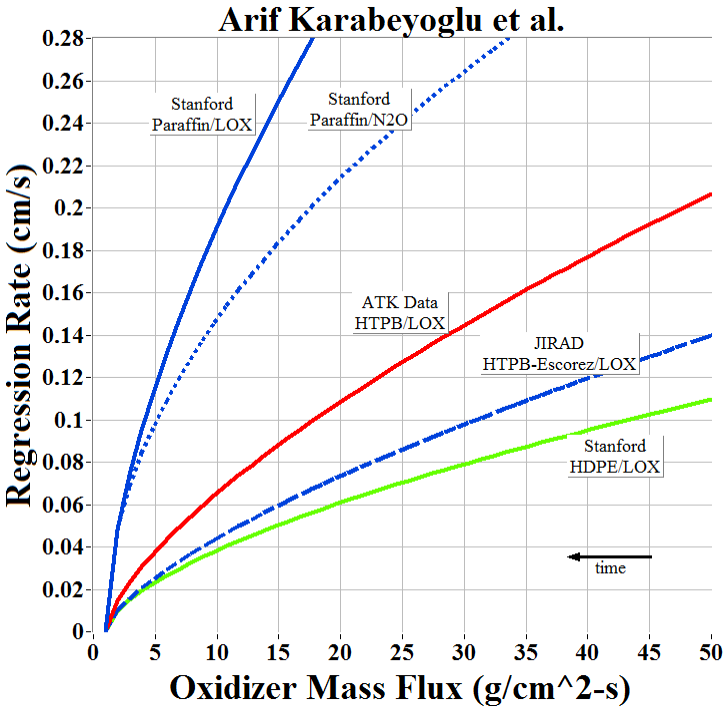

Paraffin/LOX
$\dot{r} = 0.05G_{ox}^{0.62}$

Paraffin/N2O
$\dot{r} = 0.05G_{ox}^{0.50}$

HTPB/LOX
$\dot{r} = 0.02G_{ox}^{0.68}$

HTPB-Esc./LOX
$\dot{r} = 0.01G_{ox}^{0.68}$

HDPE/LOX
$\dot{r} = 0.01G_{ox}^{0.62}$

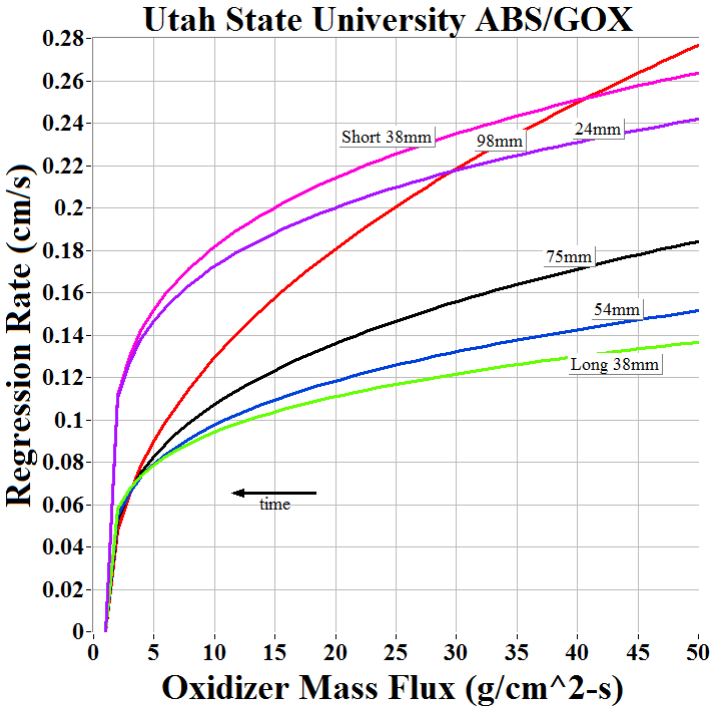

Short 38mm
$\dot{r} = 0.11G_{ox}^{0.22}$

98mm
$\dot{r} = 0.05G_{ox}^{0.45}$

24mm
$\dot{r} = 0.11G_{ox}^{0.20}$

75mm
$\dot{r} = 0.05G_{ox}^{0.32}$

54mm
$\dot{r} = 0.06G_{ox}^{0.26}$

Long 38mm
$\dot{r} = 0.06G_{ox}^{0.22}$

O/F Ratio Data from Curve-Fit Regression Rate

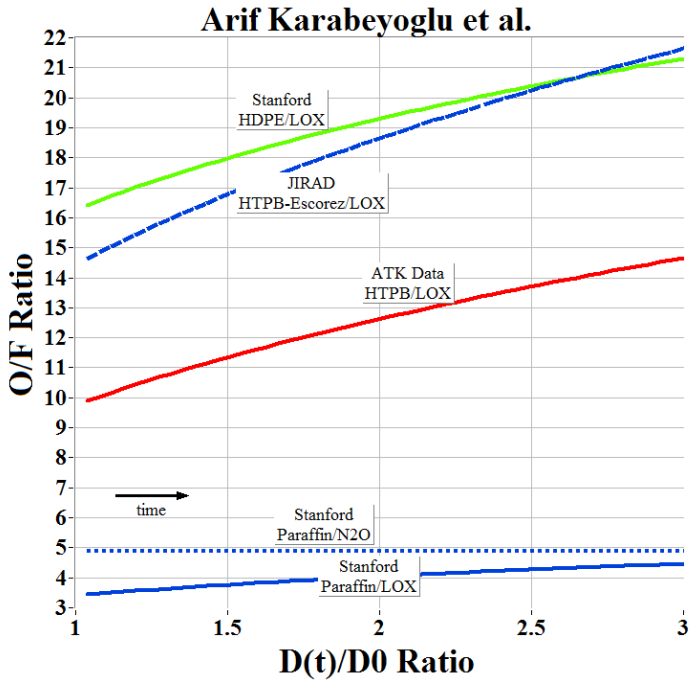

Paraffin/LOX
$\dot{r} = 0.05G_{ox}^{0.62}$

Paraffin/N2O
$\dot{r} = 0.05G_{ox}^{0.50}$

HTPB/LOX
$\dot{r} = 0.02G_{ox}^{0.68}$

HTPB-Esc./LOX
$\dot{r} = 0.01G_{ox}^{0.68}$

HDPE/LOX
$\dot{r} = 0.01G_{ox}^{0.62}$

Burn exponents are ≥ 0.5

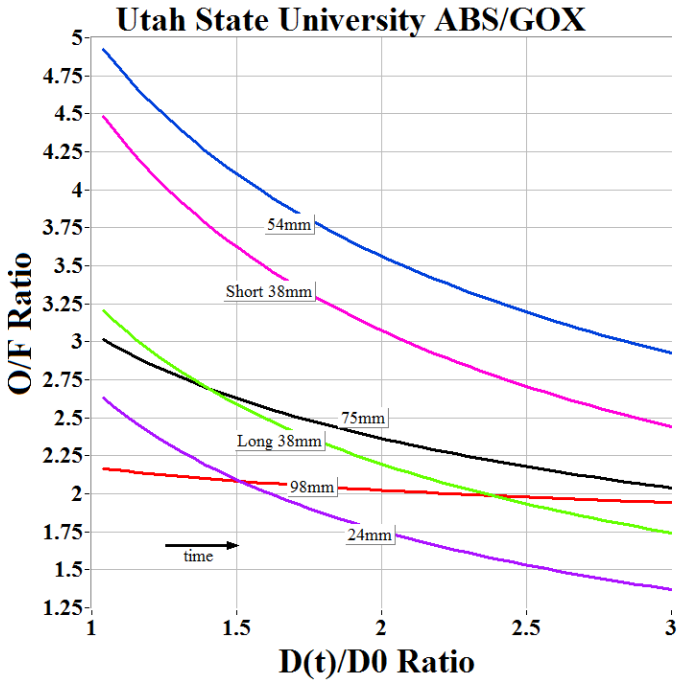

Short 38mm
$\dot{r} = 0.11G_{ox}^{0.22}$

98mm
$\dot{r} = 0.05G_{ox}^{0.45}$

24mm
$\dot{r} = 0.11G_{ox}^{0.20}$

75mm
$\dot{r} = 0.05G_{ox}^{0.32}$

54mm
$\dot{r} = 0.06G_{ox}^{0.26}$

Long 38mm
$\dot{r} = 0.06G_{ox}^{0.22}$

Burn exponents are < 0.5

O/F Ratio Analysis

- By looking at the ratio between O/F to initial O/F – expressed as $(O/F)_0$ – we can obtain the O/F ratio as a function of fuel port diameter

1. $$\frac{O/F}{(O/F)_0} = \frac{\dot{m}_{ox}}{\dot{m}_f}\left(\frac{\dot{m}_{f_0}}{\dot{m}_{ox}}\right) = \frac{\dot{m}_{f_0}}{\dot{m}_f} = \frac{\rho_f \dot{r}_0 A_{b_0}}{\rho_f \dot{r} A_b} = \frac{\dot{r}_0 D_0}{\dot{r} D} = \frac{aG_{ox_0}^n D_0}{aG_{ox}^n D} = \left(\frac{D}{D_0}\right)^{2n-1}$$

2. $$(O/F)_0 = \frac{\dot{m}_{ox}}{\dot{m}_{f_0}} = \frac{\dot{m}_{ox}}{\rho_f A_{b_0} \dot{r}_0} = \frac{\dot{m}_{ox}}{\rho_f \pi D_0 L\left(aG_{ox_0}^{\ n}\right)} = \frac{\dot{m}_{ox}^{1-n}}{\rho_f \pi^{1-n} 4^n L a} D_0^{2n-1}$$

3. $$O/F = \frac{\dot{m}_{ox}^{1-n}}{\rho_f \pi^{1-n} 4^n L a} D_0^{2n-1}\left(\frac{D}{D_0}\right)^{2n-1} = \frac{G_{ox_0}^{\ 1-n}}{4a\rho_f}\left(\frac{D_0}{L}\right)\left(\frac{D}{D_0}\right)^{2n-1}$$

Constant

Variable

Burn Exponent on O/F Ratio Shift

- O/F ratio shift is governed by the burn exponent, $O/F \propto \left(\frac{D_p}{D_{p_0}}\right)^{2n'-1}$

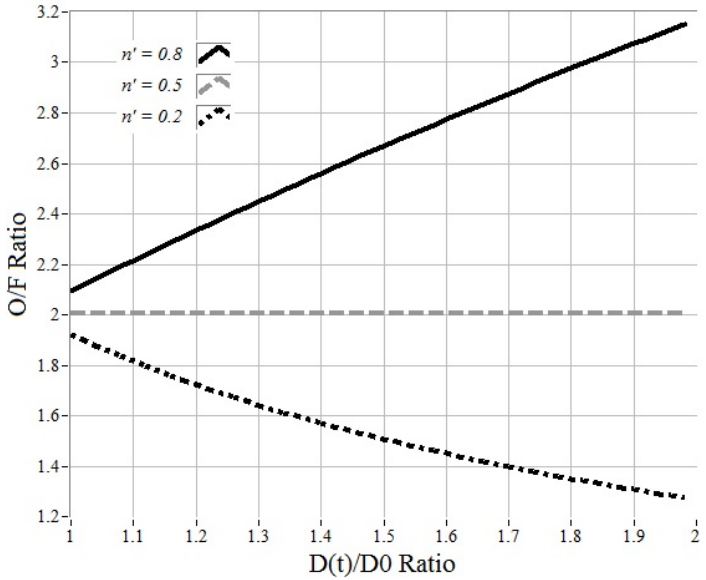

Effect on O/F Ratio Shift for Different Burn Exponent Values

- For $n' = 0.5$
  - O/F ratio is constant
- For $n' > 0.5$
  - O/F ratio increases as port diameter D increases
- For $n' < 0.5$
  - O/F ratio decreases as port diameter D increases

Qualitative Observations Match Quantitative Analysis

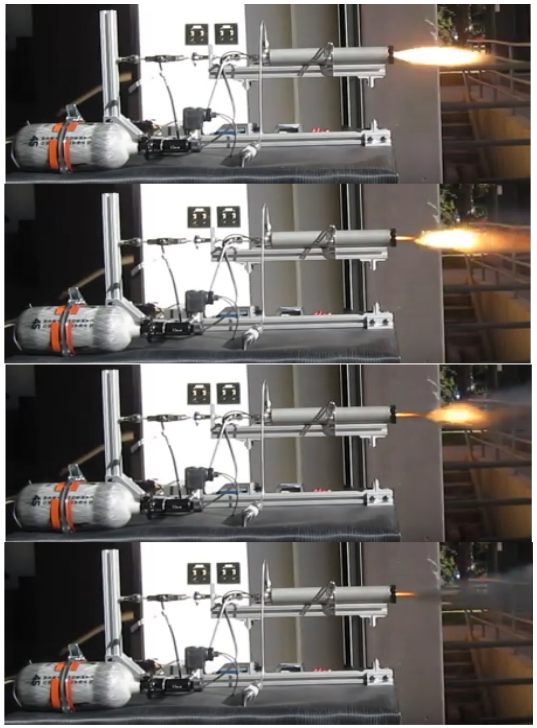

Visibly Fuel-Rich Exhaust Plume

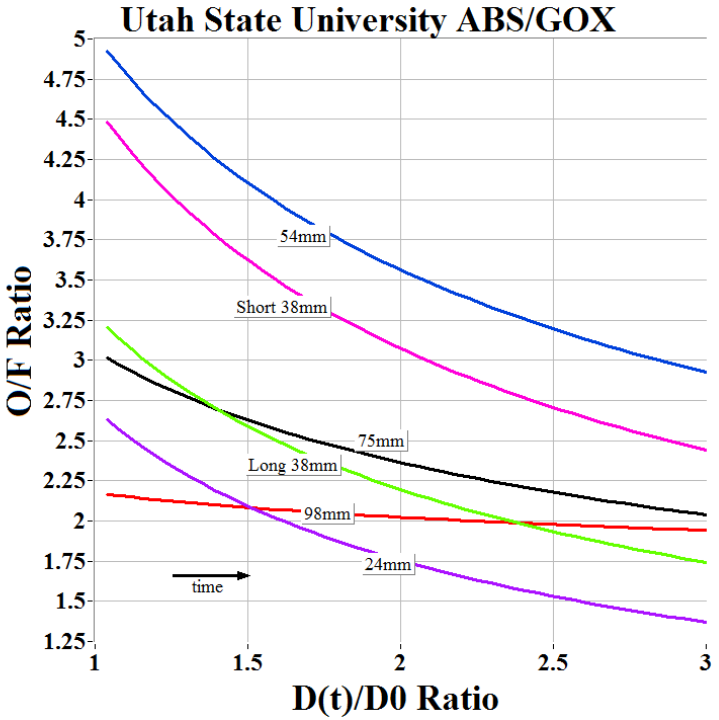

Decreasing O/F Ratio

Burn Exponent on Decreasing Motor Sizes

- Burn exponent deviates further from 0.5 with decreasing motor diameter – the smaller the motor, the more aggressive the fuel-rich O/F ratio shift

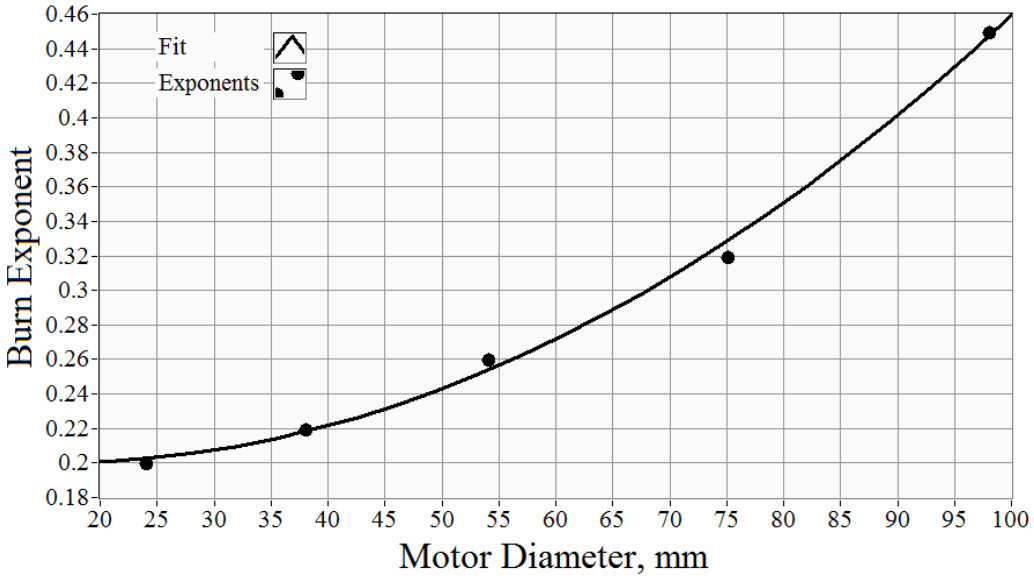

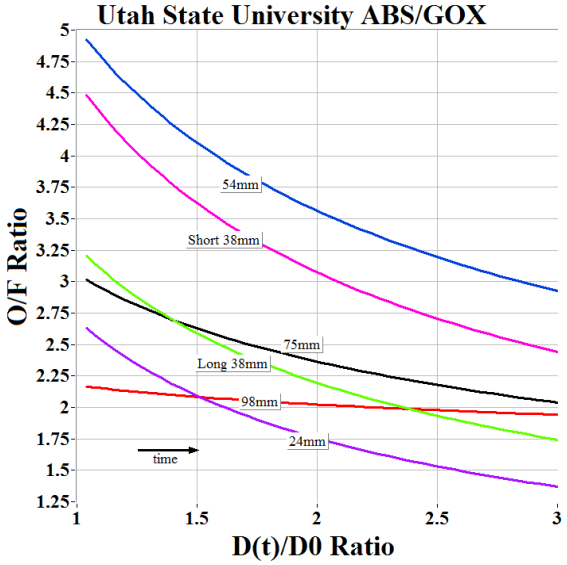

Cause of Fuel-Rich O/F Ratio

- What is the driving mechanism causing the fuel-rich tendencies seen in small-scale ABS/GOX hybrid rocket motors
- Small-scale motors come with small mass flux levels

Mass Flux Level	Low	Medium	High
Description	Radiative heat transfer dominates due to optical transmissivity of propellant particles	Convective diffusion dominates as well as fully turbulent heat and mass transfer	Gas-phase kinetics on chemical reactions become more apparent

Credit: Sutton and Biblarz, Rocket Propulsion Elements, 8th ed., pg. 601

- This investigation will demonstrate that the observed anomalous fuel-rich behavior is a result of neglected radiation terms that become dominant at small motor scales

Radiation Heating Effects

- Lower mass flux levels within small-scale motors are no longer dominated by fluid mechanics alone, but also by radiation heat transfer

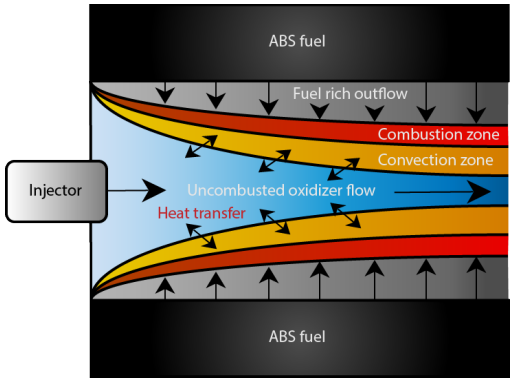

Combustion Chamber Concept for Medium Mass Flux Levels

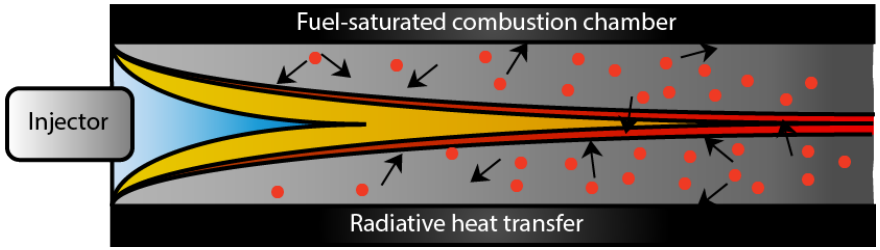

Combustion Chamber Concept for Low Mass Flux Levels

- The effect of radiation heat transfer amplifies as the combustion chamber becomes saturated with fuel particles, continuing until the solid fuel is depleted

Assessing Radiation Heating Effects

- Since the fuel regression rate drives the O/F ratio shift, the mechanisms governing regression rate need to be reconsidered

- Namely, deriving a fuel regression rate model that accounts for radiation heat transfer

- If the proposed model accurately predicts the behavior of small-scale ABS/GOX hybrid rocket motors, the hypothesis of the fuel-rich O/F ratio shift being due to radiation heat transfer effects holds a level of merit

The Marxman Fuel Regression Rate Model

- Marxman and Gilbert – pioneers of hybrid rocket theory
- Marxman's theory identifies the factors that influence fuel regression rate

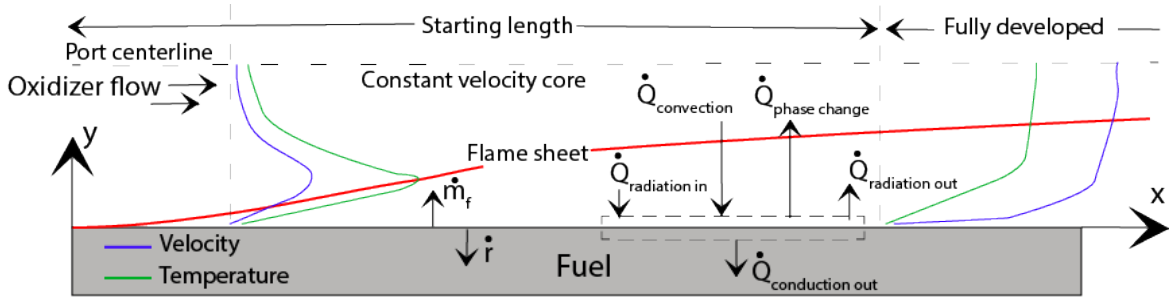

- Combustion is governed by a diffusion flame where the fuel and oxidizer mix
- Fuel regression rate is derived through an enthalpy balance

Enthalpy Balance Model (1)

- The classic Marxman model equates the enthalpy of fuel gasification to the enthalpy due to convection

$$\dot{Q}_g = \dot{Q}_c$$

  - For the scale he was considering, Marxman modeled the fluid mechanics very well

- The proposed augmented Marxman model equates the enthalpy of fuel gasification to the enthalpy due to convection **and** radiation

$$\dot{Q}_g = \dot{Q}_c + \dot{Q}_r$$

  - However, Marxman's original model is incomplete for smaller motor scales

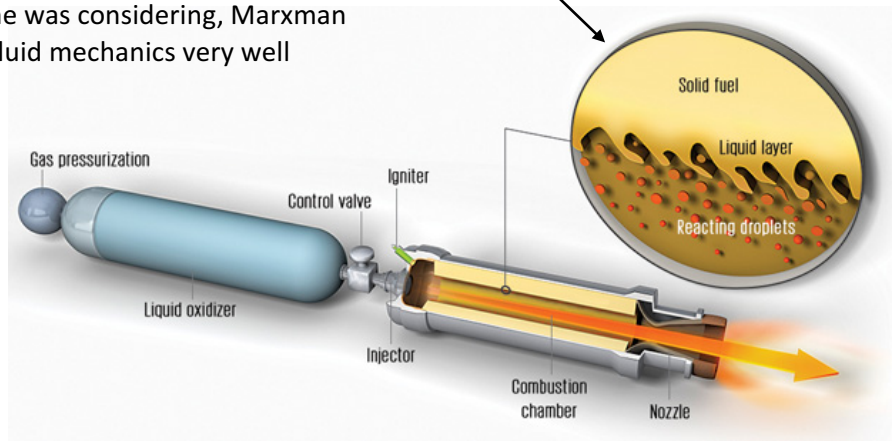

Credit: Emily Cooper and Brian Cantwell – Hybrid Rocket Concept

Enthalpy Balance Model (2)

- Classical Marxman Model – $\dot{Q}_g = \dot{Q}_c$
- Augmented Marxman Model – $\dot{Q}_g = \dot{Q}_c + \dot{Q}_r$

Power Flux (W/m^2)	Equation	Variables
Gasification	$\dot{Q}_g = \rho_f \dot{r} h_v$	ρ_f ⇒ fuel density $\dot{r}$ ⇒ fuel regression rate h_v ⇒ fuel latent heat
Convection	$\dot{Q}_c = S_t \rho_e U_e c_{p_e} (T_0 - T_f)$	S_t ⇒ Stanton Number ρ_e ⇒ combustion product density U_e ⇒ combustion product velocity c_{p_e} ⇒ combustion product specific heat T_0 ⇒ combustion chamber temperature T_f ⇒ fuel grain temperature
Radiation	$\dot{Q}_r = \sigma(\epsilon T_0^4 - \alpha T_f^4)$	σ ⇒ Stefan Boltzmann constant ϵ ⇒ emissivity of combustion plume α ⇒ absorptivity of fuel grain surface

Enthalpy Balance Model (3)

- Stanton Number – S_t
- Reynolds-Colburn analogy – $S_t = \frac{1}{2} C_{f_x} P_r^{-\frac{2}{3}}$
  - Need to account for "Wall Blowing"
  - Radially emanating flow from fuel surface pushes combustion zone away from the wall
- Lee's Model – $\frac{(C_{f_x})_B}{C_{f_x}} = \frac{1.27}{\beta^{0.77}} \quad \left(\beta = \frac{2\dot{r}\rho_f}{G_{ox} C_{f_x}}\right)$
- Boardman's approximation – $\beta = \frac{\Delta h}{h_v}$
- Stanton Number – $S_t = \frac{0.635 C_{f_x}}{P_r^{\frac{2}{3}} \beta^{0.77}}$

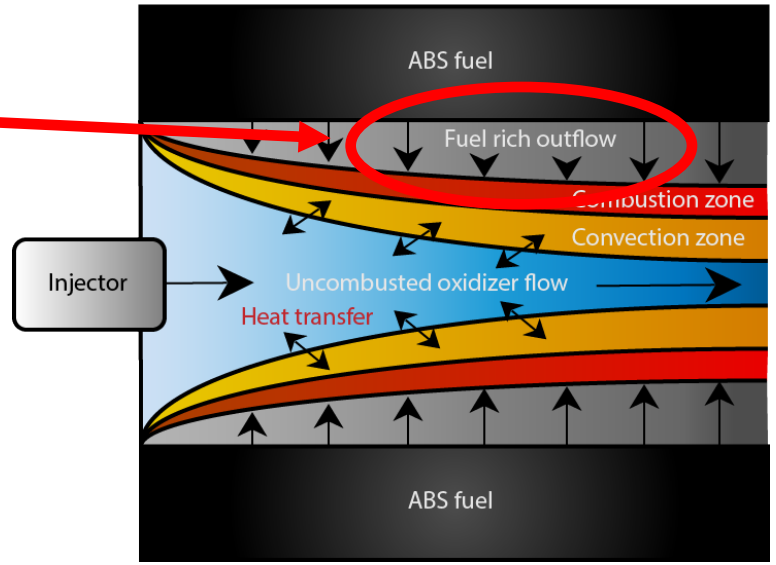

Enthalpy Balance Model (4)

- Skin Friction Coefficient – C_{f_x}
- Blasius Formula – $C_{f_x} \propto \frac{1}{R_{e_x}^{1-n}}$
- Turbulent flow at low Reynolds numbers in the presence of bypass
- Classic Marxman theory – $n = \frac{4}{5}$
- $C_{f_x} = \tau R_{e_x}^{-\frac{1}{5}} = \tau \left(\frac{\rho_e u_e x}{\mu}\right)^{-\frac{1}{5}} = \tau G_{ox}^{-\frac{1}{5}} \left(\frac{\mu}{x}\right)^{\frac{1}{5}}$

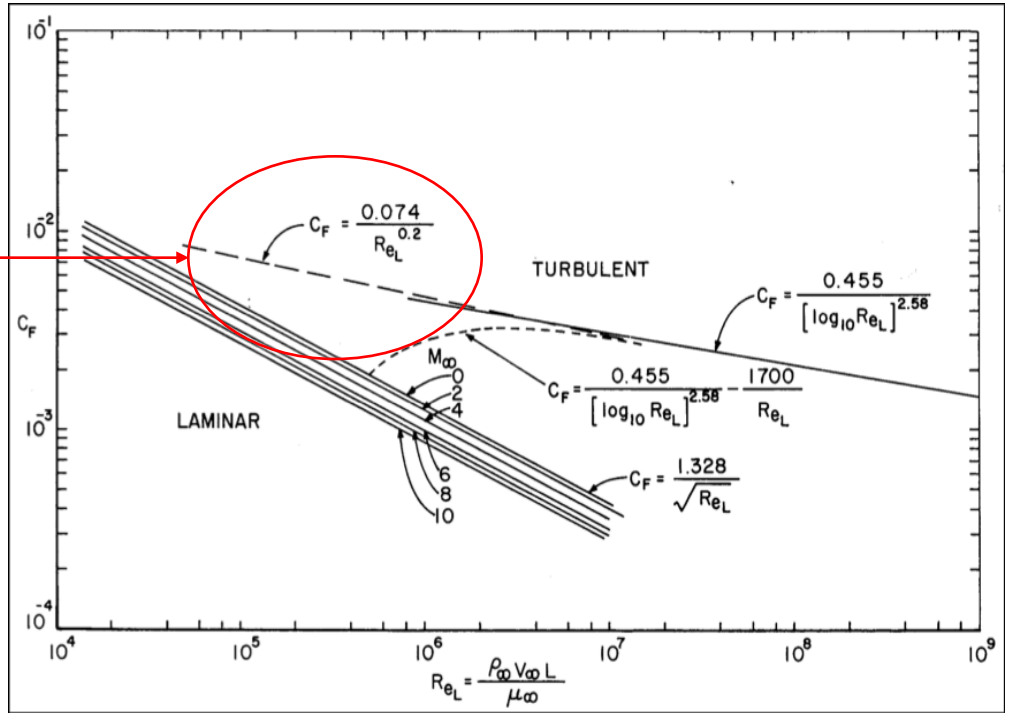

Enthalpy Balance Model (5)

$$\dot{Q}_g = \dot{Q}_c$$

$$\dot{r}\rho_f h_v = S_t \rho_e u_e \Delta h$$

$$\dot{r} = \frac{S_t \rho_e u_e \Delta h}{\rho_f h_v}$$

$$\dot{r} = \frac{0.635 C_{f_x}}{P_r^{\frac{2}{3}} \beta^{0.77}} \left(\frac{G_{ox} \Delta h}{\rho_f h_v} \right)$$

$$\dot{r} = \frac{0.635 \tau G_{ox}^{\frac{4}{5}}}{\rho_f P_r^{\frac{2}{3}} \beta^{0.77}} \left(\frac{\Delta h}{h_v} \right) \left(\frac{\mu}{x} \right)^{\frac{1}{5}}$$

- Classical Marxman Model –

$$\dot{r} = \frac{0.794 \tau G_{ox}^{\frac{4}{5}}}{\rho_f P_r^{\frac{2}{3}} \beta^{0.77}} \left(\frac{\Delta h}{h_v} \right) \left(\frac{\mu}{L} \right)^{\frac{1}{5}}$$

- Augmented Marxman Model –

$$\dot{r} = \frac{0.794 \tau G_{ox}^{\frac{4}{5}}}{\rho_f P_r^{\frac{2}{3}} \beta^{0.77}} \left(\frac{\Delta h}{h_v} \right) \left(\frac{\mu}{x} \right)^{\frac{1}{5}} + \frac{\sigma \left(\epsilon T_0^4 - \alpha T_f^4 \right)}{\rho_f h_v}$$

Regression rate due to convection

Regression rate due to radiation

Enthalpy Balance Model (6)

- Iterative model – iterate Lee's blowing coefficient (β)
- Serves as a correction when accounting for fuel-rich flow

Initial Iteration	
$\dot{\boldsymbol{r}}^{(\mathbf{0})} = \left(\frac{0.794\tau}{\rho_f P_r^{\frac{2}{3}}}\right)\left(\frac{\Delta h}{h_v}\right)\left(G_{ox}^{\frac{4}{5}}\left(\frac{\mu}{L}\right)^{\frac{1}{5}}\right)\left(\frac{1}{\boldsymbol{\beta}^{(\mathbf{0})}}\right)^{0.77} + \frac{\sigma\left(\epsilon T_0^4 - \alpha T_f^4\right)}{\rho_f h_v}$	$\boldsymbol{\beta}^{(\mathbf{0})} = \frac{\Delta h}{h_v}$
Proceeding Iterations ($\boldsymbol{j} = \{\mathbf{0}, \mathbf{1}, \mathbf{2}, \ldots\}$)	
$\dot{\boldsymbol{r}}^{(\boldsymbol{j}+\mathbf{1})} = \left(\frac{0.794\tau}{\rho_f P_r^{\frac{2}{3}}}\right)\left(\frac{\Delta h}{h_v}\right)\left(G_{ox}^{\frac{4}{5}}\left(\frac{\mu}{L}\right)^{\frac{1}{5}}\right)\left(\frac{1}{\boldsymbol{\beta}^{(\boldsymbol{j})}}\right)^{0.77} + \frac{\sigma\left(\epsilon T_0^4 - \alpha T_f^4\right)}{\rho_f h_v}$	$\boldsymbol{\beta}^{(\boldsymbol{j})} = \frac{2\rho_f P_r^{\frac{2}{3}} \dot{\boldsymbol{r}}^{(\boldsymbol{j})}}{\left(2 - \frac{4}{5}\right)\tau G_{total}^{\frac{4}{5}}\left(\frac{\mu}{L}\right)^{\frac{1}{5}}}$

Algorithm Flow Diagram

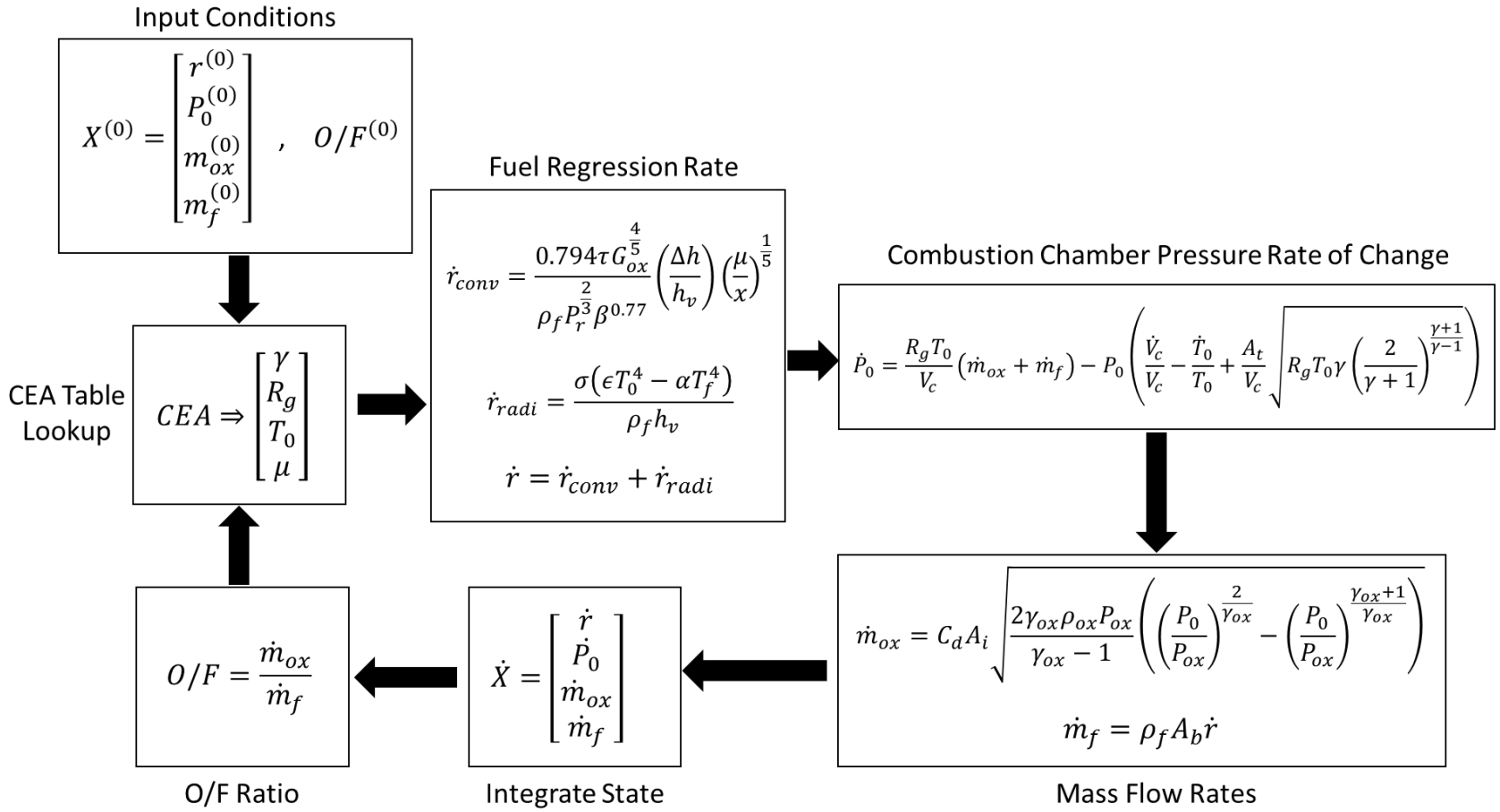

Experimental Test Set-Up

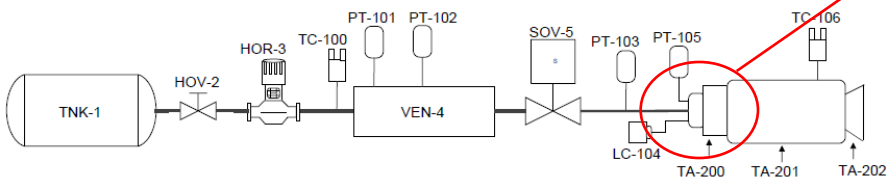

GOX Components	Functional Description
TNK-1	GOX supply tank (2000psi)
HOV-2	GOX supply on/off hand-operated valve
HOR-3	GOX hand-operated pressure reducing regulator
VEN-4	GOX Venturi flow meter
SOV-5	GOX solenoid run valve

Test Article	Functional Description
TA-200	GOX injector cap
TA-201	Motor case
TA-202	Nozzle cap

Sensors	Functional Description
TC-100	Venturi inlet temperature
PT-101	Venturi inlet pressure
PT-102	Venturi differential pressure
PT-103	GOX injector pressure
LC-104	Thrust stand load cell
PT-105	Combustion chamber pressure
TC-106	Motor case temperature

Acronyms
- TNK: tank
- HOV: hand-operated valve
- HOR: hand-operated regulator
- VEN: Venturi flow meter
- SOV: solenoid valve
- TA: test article
- TC: thermocouple
- PT: pressure transducer
- LC: load cell

Injector flow is choked

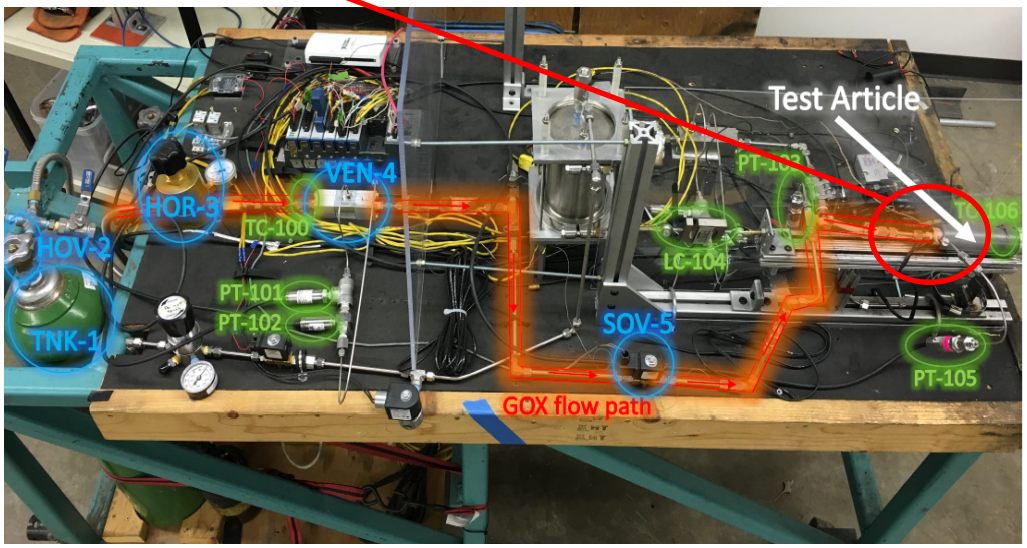

Tested Motor Configurations

1

2

3

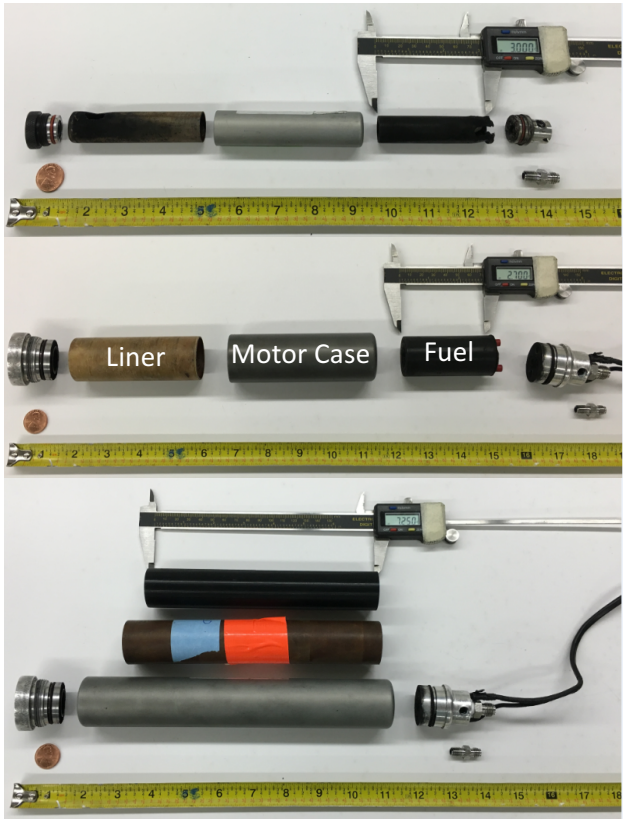

- 24mm (0.945”) motor case diameter
- 3” fuel grain length

- 38mm (1.50”) motor case diameter
- 2.7” fuel grain length

- 38mm (1.50”) motor case diameter
- 7.25” fuel grain length

Model Validation

- All three fuel regression rate models were simulated and compared to experimentally-obtained data
  - Augmented Marxman Model $\dot{r} = \frac{0.794\tau G_{ox}^{\frac{4}{5}}}{\rho_f P_r^{\frac{2}{3}} \beta^{0.77}} \left(\frac{\Delta h}{h_v}\right) \left(\frac{\mu}{x}\right)^{\frac{1}{5}} + \frac{\sigma\left(\epsilon T_0^4 - \alpha T_f^4\right)}{\rho_f h_v}$
  - Classical Marxman Model $\dot{r} = \frac{0.794\tau G_{ox}^{\frac{4}{5}}}{\rho_f P_r^{\frac{2}{3}} \beta^{0.77}} \left(\frac{\Delta h}{h_v}\right) \left(\frac{\mu}{L}\right)^{\frac{1}{5}}$
  - Empirical Curve-Fit Model $\dot{r} = a G_{ox}^{n'}$

Adjustable Parameters

- Two parameters were adjusted in order to optimize criteria
- Criteria: minimize deviation of simulated values from measured values, including
  - Chamber pressure
  - Fuel mass consumed
  - Port diameter expansion
- Adjusted parameters,
  - Optical emissivity, ϵ
  - Skin friction scale factor, τ

$$\dot{r} = \frac{0.794\tau G_{ox}^{\frac{4}{5}}}{\rho_f P_r^{\frac{2}{3}} \beta^{0.77}} \left(\frac{\Delta h}{h_v}\right) \left(\frac{\mu}{x}\right)^{\frac{1}{5}} + \frac{\sigma(\epsilon T_0^4 - \alpha T_f^4)}{\rho_f h_v}$$

Best Fit Values of τ and ϵ

- Different best-fit values of τ and ϵ were obtain per motor configuration

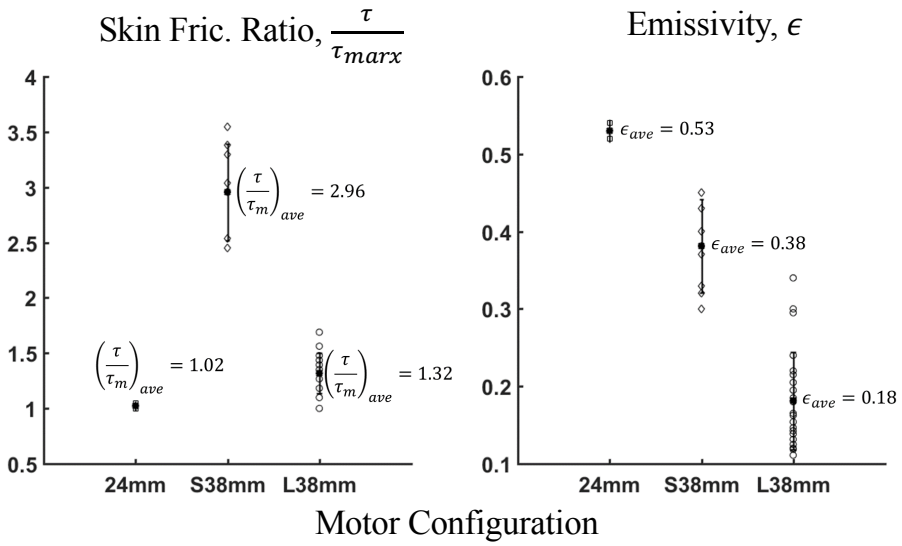

Average Adjusted Parameters with Error Bars Representing One Standard Deviation per Motor Configuration

$$\dot{r} = \frac{0.794\tau G_{ox}^{\frac{4}{5}}}{\rho_f P_r^{\frac{2}{3}} \beta^{0.77}} \left(\frac{\Delta h}{h_v}\right) \left(\frac{\mu}{x}\right)^{\frac{1}{5}} + \frac{\sigma(\epsilon T_0^4 - \alpha T_f^4)}{\rho_f h_v}$$

- $\tau_{marx} = 0.0592$

Motor	No. of Tests (Sample Size)	$x - \frac{t_{\frac{c}{2},\nu}\sigma}{\sqrt{n}} \leq \tau_{ave} \leq x + \frac{t_{\frac{c}{2},\nu}\sigma}{\sqrt{n}}$	$x - \frac{t_{\frac{c}{2},\nu}\sigma}{\sqrt{n}} \leq \epsilon_{ave} \leq x + \frac{t_{\frac{c}{2},\nu}\sigma}{\sqrt{n}}$
24mm	2	0.0428 < **0.061** < 0.0784	0.402 < **0.530** < 0.657
S38mm	8	0.1533 < **0.175** < 0.1967	0.331 < **0.381** < 0.431
L38mm	23	0.0734 < **0.078** < 0.0827	0.154 < **0.182** < 0.208

Average Adjusted Parameters within a Student-t 95% Confidence Level per Motor Configuration

Chamber Pressure Profiles

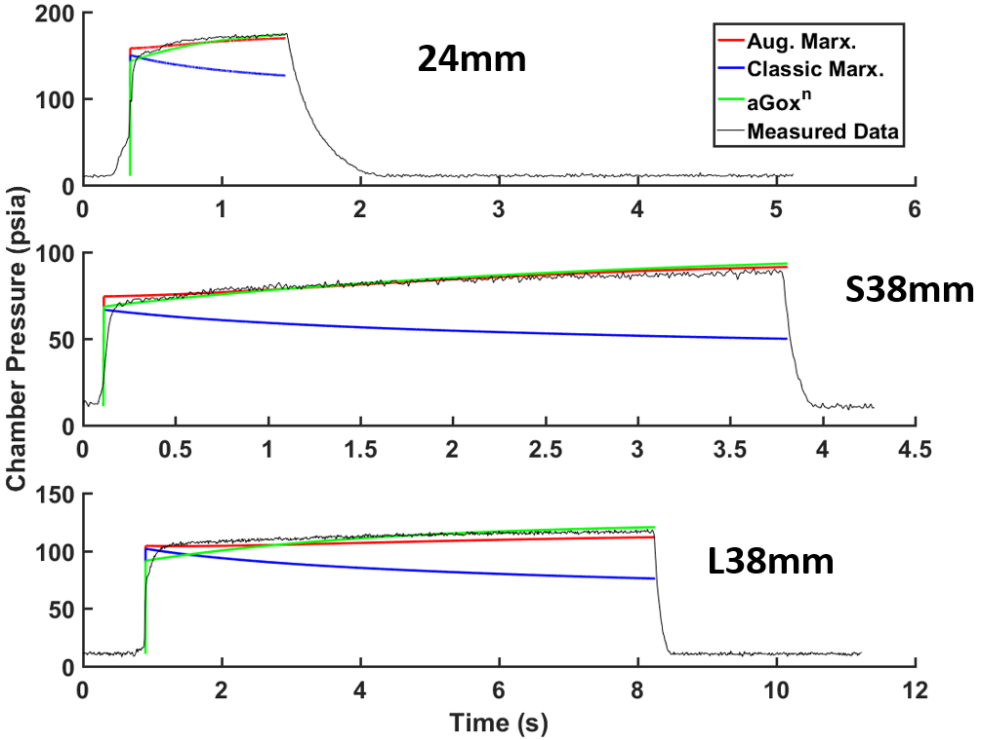

Comparison of Measured-to-Simulated Chamber Pressure using Varying Regression Rate Models per Motor Configuration

- Augmented Marx. model matches both experimental chamber pressure values as well as trend
- Classical Marx. model under-predicts experimental chamber pressure values and incorrectly predicts the trend

Accumulated Chamber Pressure Profile Error

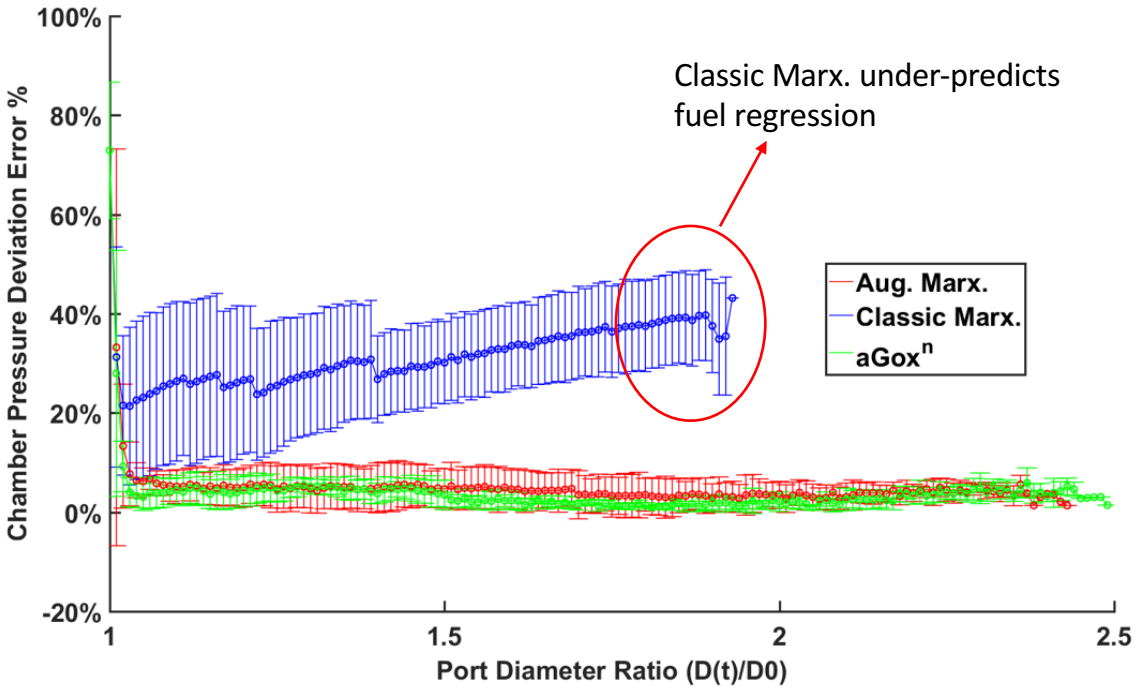

Measured-to-Simulated Chamber Pressure Profile RMSE Percentage as a Function of Port Diameter Ratio Encompassing All Tests Across All Motors

- RMSE percentage of chamber pressure across all tests
- $\%P_{0_{err}} = 100\left(\frac{|P_{0_{measured}} - P_{0_{simulated}}|}{P_{0_{measured}}}\right)$
- Chamber pressure deviation error is within 4-7% regarding the Augmented Marx. model
- Chamber pressure deviation error regarding the Classical Marx. model continue to increase as port diameter expands

Mass and Diameter Error Per Test

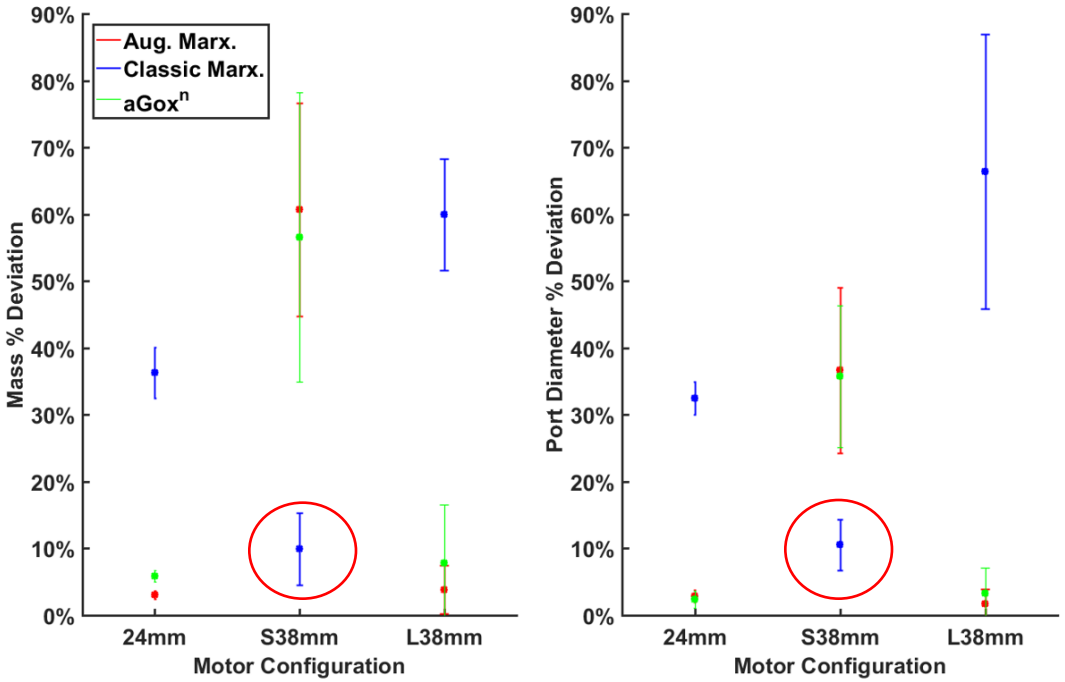

Average Measured-to-Simulated Percent Mass and Port Diameter Deviation per Motor Configuration

- Where the Classical Marx. model normally under-predicts fuel mass consumed and port diameter expansion, it predicts these parameters more accurately for the S38mm motor configuration
- May be an artifact of the smaller length-to-diameter ratio of the S38mm motor configuration

Motor	L/D Ratio
24mm	3.19
S38mm	1.79
L38mm	4.85

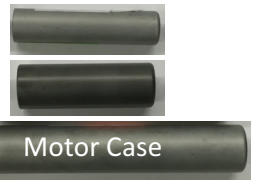

Discussion of Results

$$\dot{r} = \frac{0.794\tau G_{ox}^{\frac{4}{5}}}{\rho_f P_r^{\frac{2}{3}} \beta^{0.77}} \left(\frac{\Delta h}{h_v}\right) \left(\frac{\mu}{x}\right)^{\frac{1}{5}} + \frac{\sigma\left(\epsilon T_0^4 - \alpha T_f^4\right)}{\rho_f h_v}$$

$$\dot{r} = \dot{r}_{convection} + \dot{r}_{radiation}$$

$$\frac{\dot{r}_{radiation}}{\dot{r}_{convection}} = \frac{\frac{\sigma\left(\epsilon T_0^4 - \alpha T_f^4\right)}{h_v}}{\left(\frac{1}{G_{ox}^{\frac{4}{5}}}\right)\left(\frac{0.794\tau}{P_r^{\frac{2}{3}}} \left(\frac{\Delta h}{h_v}\right) \left(\frac{\mu}{L}\right)^{\frac{1}{5}} \left(\frac{1}{\beta^{0.77}}\right)\right)}$$

- At low oxidizer mass flux levels (G_{ox}), the radiation term dominates – tending towards a fuel-rich burn
- At high oxidizer mass flux levels, the convection term dominates – tending towards a fuel-lean burn
- The Stanton number exponent, n, remains at 4/5, indicating that the classic Marxman theory still hold true
- It describes the fluid mechanics within hybrid rocket motors, but is incomplete with regards to smaller mass flux levels

In Eq. (24) the ratio of the radiative-to-convective heat transfer terms is

$$R/C = \frac{\left(\frac{\pi}{4}D^2\frac{1}{\dot{m}_{ox}}\right)\left(\frac{\sigma_{Bolz}\cdot\left(\varepsilon\, T_0^4 - \alpha\, T_f^4\right)}{h_v}\right)}{\left(\frac{0.635}{P_r^{2/3}}\frac{\tau}{n}\right)\left(\frac{\Delta h_{flame/fuel}}{h_v}\right)\left(\frac{\mu}{L}\right)^{1-n}\left(\frac{1}{\overline{\beta}}\right)^{0.77}} = \frac{\frac{1}{\overline{G}_{ox}{}^{n}}\left(\frac{\sigma_{Bolz}\cdot\left(\varepsilon\, T_0^4 - \alpha\, T_f^4\right)}{h_v}\right)}{\left(\frac{0.635}{P_r^{2/3}}\frac{\tau}{n}\right)\left(\frac{\Delta h_{flame/fuel}}{h_v}\right)\left(\frac{\mu}{L}\right)^{1-n}\left(\frac{1}{\overline{\beta}}\right)^{0.77}} \quad (13).$$

Thus, the relative importance of the radiation term is inversely proportional to the oxidizer massflux. Also, further examination of Eq. (25) shows that as the oxidizer massflow grows the radiative heating term diminishes until Eq. (26) reduces to

$$O/F = \frac{\left(\frac{4}{\pi}\dot{m}_{ox}\right)^{1-n} D^{2n-1}}{(4\,L)\left[\left(\frac{0.635}{P_r^{2/3}}\frac{\tau}{n}\right)\left(\frac{\Delta h_{flame/fuel}}{h_v}\right)\left(\frac{\mu}{L}\right)^{1-n}\left(\frac{1}{\overline{\beta}}\right)^{0.77}\right]}. \quad (14)$$

and the D^{2n-1} term in the numerator forces the previously described lean *O/F* shift as the fuel port opens up, for $n > 1/2$. In contrast for low mass flows the radiative term grows, and at very low massflow levels

$$O/F = \frac{\left(\frac{4}{\pi}\dot{m}_{ox}\right)^{1-n} D^{2n-1}}{(4\,L)\left[\left(\frac{\pi}{4}D^2\frac{1}{\dot{m}_{ox}}\right)\left(\frac{\sigma_{Bolz}\cdot\left(\varepsilon\, T_0^4 - \alpha\, T_f^4\right)}{h_v}\right)\right]} = \frac{\left(\frac{1}{\pi}\frac{\dot{m}_{ox}}{D\,L}\right)}{\left(\frac{\sigma_{Bolz}\cdot\left(\varepsilon\, T_0^4 - \alpha\, T_f^4\right)}{h_v}\right)}. \quad (15)$$

Qualitative analysis of Eqs. (24) and (25) suggests that when the motor is operating at low oxidizer mass flux levels, the radiation term dominates – tending towards a fuel-rich burn. At high oxidizer mass flux levels, the convection term dominates – tending towards a fuel-lean burn. This predicts the contradictory result between the O/F ratio shifts between small-scale ABS/GOX HRMs and HRMs using different propellants at higher oxidizer mass fluxes as shown in Figure 3b. As such, the low burn exponents can be explained as a result of non-negligible radiative heat transfer. In summary the following qualitative observations can be made,

1. *For $n > 1/2$* the *convective term gets "leaner" with time as D grows, and the radiation term always gets "Richer" with time as D grows,*
2. *For $n < 1/2$* the *convective term gets "richer" with time as D grows, and the radiation term always gets "Richer" with time as D grows,*
3. *At low massflux levels radiation terms dominate tending towards a rich burn,*

4. *At higher massflux levels convective term tends to dominate tending towards a lean burn!*

This analysis agrees with the behavior observed during the previously described testing campaign, and offers a plausible explanation for the observed scale effects presented by Figs. (2) through (5). The small motors tested generally produced higher massflux levels due to the small initial port size; thus, the tendency towards lean-to-rich O/F shifts.

V. Test Apparatus for Augmented Marxman Model Verification Tests

The test data collected to evaluate the analytical models of the previous section focused primarily on the small motor configurations *{4, 5, 6}* of Table 2, since these motors showed the greatest propensity for a fuel-rich O/F shift during the burn lifetime. Respectively these configurations were named as 38-short (*S38mm*), 38-long (*L38mm*), and *24mm*, based on the outer case diameter and the motor length. Images on the Right hand side of Figure 9 display the motor layout for the small-scale motors. Figure 9 also shows a detailed internal schematic of the 38-short (*S38mm*) configuration. The hardware for these test configurations consisted of a nozzle cap, motor case, insulating liner, fuel grain, injector cap, and adapter fitting for a pressure transducer. The other detailed thrust chamber layouts are very similar. The majority of the verification tests were performed with the *L38mm* configuration (*23*); with an additional *8 burns* performed using the *S38mm*, and *6 burns* of the *24mm* configurations. A total of 37 small motor runs were performed for this evaluation campaign. The fuel grains were printed from a standard black ABS plastic industrial feed stock.

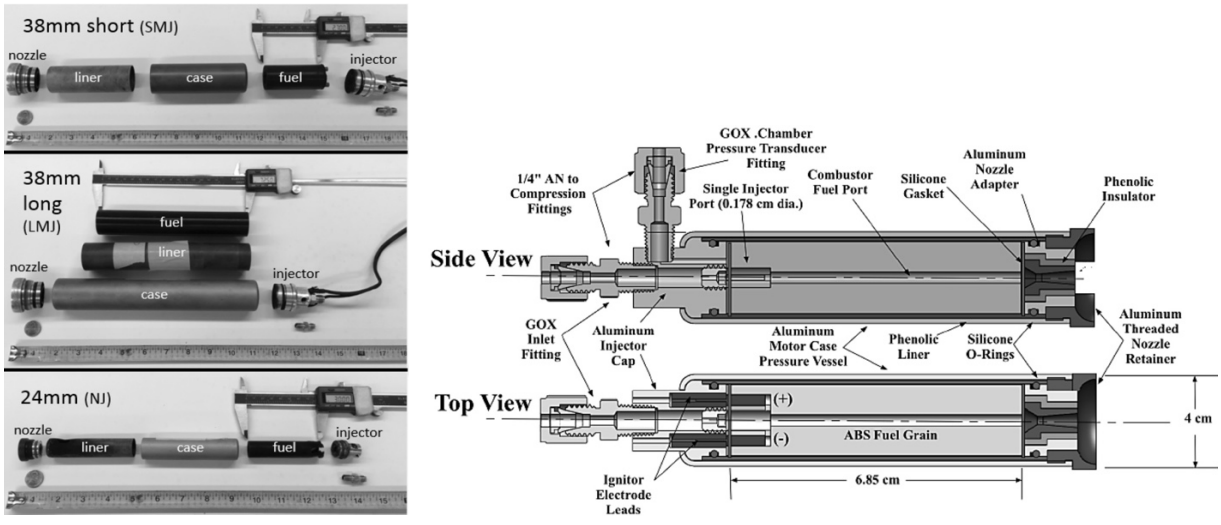

(a) Exploded Views of Motor Components **(b) Internal Motor Assembly Schematic.**

Figure 9. Exploded Views of the S38mm, L38mm, and 24mm Thrust Chamber Components.

The significant differences between the estimated emissivity and absorptivity values clearly indicate that the process is not in optical equilibrium. The relatively low estimated plume emissivity varying between approximately 0.53 and 0.15 values indicate some degree of plume opaqueness. As shown by Figure 13, this opaqueness correlates with the mean O/F ratios of the test motors.

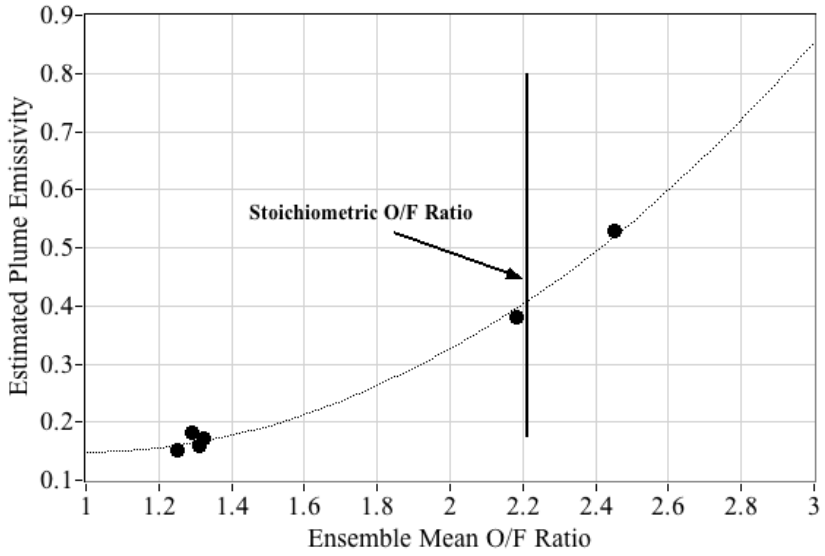

Figure 14. Effect of Ensemble Mean O/F Ratio Upon Maximum Likelihood Estimate of Plume Emissivity.

The plume does not consist of a single set of monolithic combustion products, but continuously varies from pure oxidizer at the fuel port inlet to the exit products along the length of the fuel port. Clearly, due to accumulated entrainment of pryolized fuel into the core flow stream, the highest massflux levels will occur at the end of the motor. At the top end of the motor the plume combustion products have not yet built up and the plume consists mainly of the oxidizer flow which is relatively more optically transparent. Near the aft end of the motor fuel pyrolysis products make up a larger mix of the local massflow cross section, and the plume is relatively more opaque. When the maximum likelihood analysis is applied to the longitudinal mean model, the estimated values for the emissivity and absorptivity values are simply the effective values blended over the length of the thrust chamber.

VII. Summary and Conclusion

Utah State University has developed a hybrid rocket system that uses a common industrial plastic ABS as the fuel material. The rocket fuel grains are fabricated using a type of 3-D printing known as Fused Deposition Modeling. Although ABS has been demonstrated as an effective rocket fuel, the material possesses unique burn characteristics

Conclusion

- The fuel-rich O/F ratio behavior of small-scale ABS/GOX hybrid rocket motors is an artifact of low mass flux levels
- This gives rise to a new flow regime where radiative heat transfer effects become more apparent
- The classic Marxman model that only accounts for convective heat transfer effects is insufficient in predicting low mass flux performance
- Including the effects of radiation heat transfer provides for the appropriate correction

Future Work

- Effects of motor length-to-diameter ratio requires further investigation
- Use different propellant combinations with small-scale motors
- Emissivity and skin friction scale factor dependency on port diameter

Appendix

- Extracting Regression Rate from Experimental Data
- Classical Marxman Regression Rate Derivation
- Augmented Marxman Regression Rate Derivation and Beta Derivation for Iterations
- Table Summary of Chamber Pressure Error
- Table Summary of Mass and Diameter Error
- Chamber Pressure Profile and Qualitative Comparison